









## Article

# Bacterial Cellulose Composites with Polysaccharides Filled with Nanosized Cerium Oxide: Characterization and Cytocompatibility Assessment

Valentina A. Petrova <sup>1</sup>, Iosif V. Gofman <sup>1,\*</sup>, Alexey S. Golovkin <sup>2</sup>, Alexander I. Mishanin <sup>2</sup>,  
Natallia V. Dubashynskaya <sup>1</sup>, Albert K. Khripunov <sup>1</sup>, Elena M. Ivan'kova <sup>1</sup>, Elena N. Vlasova <sup>1</sup>,  
Alexandra L. Nikolaeva <sup>1</sup>, Alexander E. Baranchikov <sup>3</sup>, Yury A. Skorik <sup>1</sup>, Alexander V. Yakimansky <sup>1</sup>  
and Vladimir K. Ivanov <sup>3</sup>

<sup>1</sup> Institute of Macromolecular Compounds, Russian Academy of Sciences, Bolshoi VO 31, St. Petersburg 199004, Russia

<sup>2</sup> Almazov National Medical Research Centre, Akkuratova 2, St. Petersburg 197341, Russia

<sup>3</sup> Kurnakov Institute of General and Inorganic Chemistry, Russian Academy of Sciences, Leninskii 31, Moscow 119071, Russia

\* Correspondence: gofman.imc@gmail.com



**Citation:** Petrova, V.A.; Gofman, I.V.; Golovkin, A.S.; Mishanin, A.I.; Dubashynskaya, N.V.; Khripunov, A.K.; Ivan'kova, E.M.; Vlasova, E.N.; Nikolaeva, A.L.; Baranchikov, A.E.; et al. Bacterial Cellulose Composites with Polysaccharides Filled with Nanosized Cerium Oxide: Characterization and Cytocompatibility Assessment. *Polymers* **2022**, *14*, 5001. <https://doi.org/10.3390/polym14225001>

Academic Editor: Roman A. Surmenev

Received: 28 September 2022

Accepted: 15 November 2022

Published: 18 November 2022

**Publisher's Note:** MDPI stays neutral with regard to jurisdictional claims in published maps and institutional affiliations.



**Copyright:** © 2022 by the authors. Licensee MDPI, Basel, Switzerland. This article is an open access article distributed under the terms and conditions of the Creative Commons Attribution (CC BY) license (<https://creativecommons.org/licenses/by/4.0/>).

**Abstract:** A new biocompatible nanocomposite film material for cell engineering and other biomedical applications has been prepared. It is based on the composition of natural polysaccharides filled with cerium oxide nanoparticles (CeONPs). The preparative procedure consists of successive impregnations of pressed bacterial cellulose (BC) with a sodium alginate (ALG) solution containing nanoparticles of citrate-stabilized cerium oxide and a chitosan (CS) solution. The presence of CeONPs in the polysaccharide composite matrix and the interaction of the nanoparticles with the polymer, confirmed by IR spectroscopy, change the network architecture of the composite. This leads to noticeable changes in a number of properties of the material in comparison with those of the matrix's polysaccharide composition, viz., an increase in mechanical stiffness, a decrease in the degree of planar orientation of BC macrochains, an increase in hydrophilicity, and the shift of the processes of thermo-oxidative destruction of the material to a low-temperature region. The latter effect is considered to be caused by the redox activity of cerium oxide (reversible transitions between the states Ce<sup>4+</sup> and Ce<sup>3+</sup>) in thermally stimulated processes in the nanocomposite films. In the equilibrium swollen state, the material retains a mechanical strength at the level of ~2 MPa. The results of in vitro tests (cultivation of multipotent mesenchymal stem cells) have demonstrated the good biocompatibility of the BC-ALG(CeONP)-CS film as cell proliferation scaffolds.

**Keywords:** nanocomposites; biopolymers; bacterial cellulose; polysaccharides; ceria nanoparticles; biomedical applications; stem cell proliferation

## 1. Introduction

Different polymer composites based on natural [1] and synthetic polymers [2] are used for tissue engineering. Polysaccharides are considered to be quite promising materials for creating scaffolds for tissue engineering due to their compatibility with human tissues, low toxicity, and ability to enhance regeneration processes. A number of polymer matrices for tissue engineering in various forms (films [3–5], different types of gels [6–13], and nonwoven materials [14–19]) have been developed using different polysaccharides. Among the great variety of polymeric materials for tissue engineering, a special place is held by bacterial cellulose (BC) [20] and BC-based composites [21].

BC, a linear, unbranched polysaccharide consisting of β-1,4-glucopyranose units, is extracellularly produced by microorganisms (*Komagataeibacter rhaeticus*) in the process of oxidative fermentation. BC consists of an ultradispersed fiber network and is characterized

by a complex hierarchical morphology along with high crystallinity. The material has a unique set of properties, such as the tendency to swell in aqueous media, excellent thermal and mechanical properties, nontoxicity, and high biocompatibility. Due to its structural similarity to the components of the extracellular matrix (for example, collagen), BC is capable of taking part in complex interactions with biological tissues. This group of properties makes BC a perspective object in the development of matrices for tissue engineering.

Both BC itself [22–24] and different BC-based composites [25] and nanocomposites [26,27] are regarded as promising materials since one can easily control their properties in a wide range. To obtain such composites, various methods have been developed for introducing polymers into the BC and fixing them in the material (adsorption of polymers, wet molding of BC dispersed in polymer solutions, BC biosynthesis in the presence of polymers, and a combination of these methods) [28–34].

The modification of BC by pressing, followed by impregnation with solutions of various polyacids (alginic or hyaluronic acids or carrageenan) and a chitosan (CS) solution leads to the formation of a polyelectrolyte network. The network architecture and properties of the material change in this process. These properties depend on the type of polyacids, their structure, and the nature of their interaction with BC and CS. For example, after drying at room temperature, the composite based on sodium alginate (ALG), in contrast to the initial BC, possesses a high water-retaining capacity and porosity and demonstrates higher cytocompatibility [21]. Thus, biocompatibility, low cytotoxicity, excellent mechanical properties (especially in the swollen state), and a highly porous structure make BC and its composites a suitable material for tissue engineering applications.

In recent years, many researchers have been engrossed in studying composite biomaterials containing nanoscale components and their use in tissue repair and regeneration. For instance, experiments on the use of cerium oxide nanoparticles (CeONPs) in tissue engineering show that composites containing CeONPs as an active filler applied as scaffolds can affect the behavior of stem cells: their migration, proliferation, and differentiation [35]. The nanostructured design of a tissue implant ensures the biocompatibility of the material, providing a close resemblance to the natural extracellular matrix and facilitating the optimal implementation of the biological factors necessary for functional tissue regeneration [36].

CeONPs can stimulate tissue regenerative activity due to their oxidative potential [35]. However, despite their antioxidant activity, CeONPs can cause oxidative stress under certain conditions [37]. To increase the efficiency and reduce the toxicity of CeONPs, they are confined in polymer matrices. The proper design of polymer-CeONP composites makes it possible to modulate the antioxidant/pro-oxidant activity of nanoparticles and enhance the antimicrobial properties of the material [38]. Recent advances in the field of biomedical polymer-CeONP composites have shown how these nanoparticles augment the biomedical potential of modern polymer materials [39–42]. Being embedded into polymer scaffolds, CeONPs influence the structure and morphology of polymeric objects, thereby determining their mechanical and thermal properties, biodegradation kinetics, porosity, and swelling capacity.

The introduction of CeONPs into the BC structure by mixing the disintegrated polysaccharide gel film and the dispersion of nanoparticles causes an increase in the stiffness of the resulting nanocomposite film, along with a decrease in its ability to swell. This indicates the formation of additional intermolecular interactions in the composite via the active surface of the nanoparticles [43]. The study of this nanocomposite film as a bioresorbable scaffold for the proliferation of mesenchymal stem cells has shown a positive effect of cerium oxide on the attachment of cells to the substrate, followed by their growth.

An analysis of both the literature data and the results previously obtained by the authors convincingly confirms the importance and future prospects of the research on the multicomponent nanocomposite materials based on an already developed combination of polysaccharides. The combination includes pressed BC, as well as ALG and CS filled with CeONPs. The development and study of such composites is, undoubtedly, of scientific and practical interest.

This paper addresses the methodology of the preparation of new nanocomposites for biomedical applications with the aforesaid composition obtained by sequential impregnations of the pressed BC with ALG and CS solutions containing CeONPs. We have studied a complex of properties of the obtained materials and determined the mutual influence of the polymer and nanofiller. The cytocompatibility of the composites has also been assessed.

## 2. Materials and Methods

### 2.1. The Biosynthesis of BC

The biosynthesis of BC was carried out under surface cultivation using a B-13015 strain of *Komagataeibacter rhaeticus* (Russian National Collection of Industrial Microorganisms), according to the previously published method [44]. The obtained BC gel film was then pressed between layers of cotton fabric on an oil press until three-fold weight loss was obtained (henceforth, wrung-out BC).

### 2.2. The Citrate-Stabilized Cerium Dioxide Nanoparticles

The citrate-stabilized cerium dioxide nanoparticles used in the experiments, ~3.5–5 nm in size, were synthesized according to the protocol described in [45].

### 2.3. Preparation of Composite Films

Sodium alginate (Qingdao Bright Moon Seaweed Group Co. Ltd., Qingdao, China) with an MW =  $1.3 \times 10^5$  [46], chitosan (Ennagram, Pantin, France) with an MW =  $1.6 \times 10^5$ , and the degree of deacetylation of 80% [47] were used in the fabrication of the nanocomposites.

A composite of BC–ALG–CS (control) was prepared by sequential impregnations of the partly pressed BC containing 10% of the dry substance with a 2% ALG solution and a 1% CS solution in acetic acid, according to a previously developed method [21].

When preparing BC–ALG(CeONP)–CS, the preliminarily obtained experimental data on the amount of ALG and CS solutions absorbed by pressed BC were taken into account (26 and 3%, correspondingly) [21].

To obtain a solution of ALG(CeONP), a 2% solution of ALG was mixed with a 2% citrate-stabilized dispersion of CeO<sub>2</sub> under constant mechanical stirring. The ALG solution was obtained with a nanofiller content of 12% of the polymer weight. BC–ALG(CeONP)–CS was fabricated according to a previously developed technique [21] of successive impregnations of pressed BC with a 2% ALG(CeONP) solution and 1% CS solution, followed by treatment with an alcohol solution of ammonia and washing with ethyl alcohol. The resulting composite film was dried at room temperature in a fixed position. Weighing was carried out at each stage of processing to determine its composition. The composite obtained consisted of BC (71.2 wt.%), ALG (25.9 wt.%), CS (2.9 wt.%), and CeONPs (3.1% of polymer weight).

To determine the nature of the effect of the citrate-stabilized CeONP dispersion on the properties of ALG, a control film was prepared from a 2% solution of ALG containing 12% CeONPs. The solution was cast from a spinneret on a glass substrate and dried at room temperature.

### 2.4. Characterization of the Control and Composite Films

Fourier-transform infrared spectroscopy (FTIR) spectra of the ALG, ALG(CeONP), and BC–ALG(CeONP)–CS films were recorded on a Vertex 70 IR Fourier spectrometer (Bruker Optics, Ettlingen, Germany). The MIRacle ATR (Attenuated Total Reflection) reflector (Pike Technologies, Madison, Fitchburg, WI, USA) with a ZnSe working element was used in order to keep the structure of the films. When registering the ATR spectra, a correction was introduced that takes into account the penetration depth depending on the wavelength [39].

Equilibrium swelling of films—swelling after 24 h of water exposure—was determined by the gravimetric method.

The resulting films were tested via scanning electron microscopy (SEM) using a SUPRA-55VP scanning electron microscope (Carl Zeiss, Oberkochen, Germany) and via

wide-angle X-ray scattering (WAXS) using a Bruker D8 DISCOVER X-ray diffractometer with  $\text{CuK}\alpha$  (Bruker, Karlsruhe, Germany). SEM images were obtained using a secondary electron detector as well as a backscattered electron detector. To visualize the distribution of CeONPs in the samples, the films were frozen and split in liquid nitrogen, and then they were glued onto a conductive tape, sputtered by a thin layer of platinum, and tested using an energy-dispersive elemental analysis (EDX) to obtain the maps of the distribution of Ce. Element maps were collected with the help of an EDX-Max 80 mm<sup>2</sup> detector (Oxford Instruments, Oxford, UK). The analysis was performed over the entire visible area of the samples.

An AG-100kNX Plus setup (Shimadzu, Osaka, Japan) operating in a uniaxial extension mode was used to study the mechanical characteristics of the films. Strip-like samples ( $2 \times 20 \text{ mm}^2$ ) were stretched at room temperature at a rate of 2 mm/min, according to ASTM D638 requirements. The stress–strain curves of the samples were registered during the tests. Young's modulus ( $E$ ), the break stress ( $\sigma_b$ ), and the ultimate deformation ( $\epsilon_b$ ) were determined.

Thermogravimetric (TGA) and differential thermal (DTA) analyses were performed to determine the concentration of the remaining water in the films and the content of cerium oxide in the nanocomposite materials, and to characterize the impact of the nanofiller on the thermal properties of the composite films. Using TGA curves, we determined the thermal stability indices of the samples,  $\tau_5$  and  $\tau_{10}$  (the temperatures at which a polymer or a composite loses 5% and 10% of its initial weight, respectively, as a result of thermal destruction processes). A DTG-60 thermal analyzer (Shimadzu, Kyoto, Japan) was used, and the samples (~5 mg) were heated in air up to 600 °C at a rate of 5 °C/min.

### 2.5. Cultivation of Multipotent Mesenchymal Stem Cells (MMSCs)

The study of the biocompatibility of the cell culture with the scaffold was conducted on BC–ALG–CS and BC–ALG(CeONP)–CS samples. Human multipotent mesenchymal stem cells (MMSCs) obtained from subcutaneous adipose tissue of healthy donors were used as a cell culture. Cover slips of 12 mm in diameter were used as a control. The study was performed according to the Helsinki Declaration and approval was obtained from the Local Ethics Committee of the Almazov National Medical Research Centre (No. 12.26/2014; 1 December 2014). Written informed consent was obtained from all subjects prior to fat tissue biopsy.

The cell culture was performed in an alpha-MEM culture medium (Thermo Fisher Scientific, Waltham, MA, USA) supplemented with 10% fetal bovine serum, 1% L-glutamine, and 1% penicillin/streptomycin solution (Thermo Fisher Scientific, Waltham, MA, USA) in a CO<sub>2</sub> incubator containing 5% CO<sub>2</sub> at 37 °C. The study was performed as it was previously described elsewhere [21]. Briefly, rectangular samples of materials  $12 \times 8 \text{ mm}^2$  in size were placed in phosphate-buffered saline (PBS) containing 2% penicillin/streptomycin solution for 30 min, and then washed three times with fresh PBS. The cover slips were treated in 70% ethanol for 10 min and then washed three times in PBS. Next, the samples and cover slips were placed in the wells of a 24-well plate. Then, 1 mL of MMSC suspension in a concentration of 50,000 cells/mL was added and cocultured for 72 h in a CO<sub>2</sub> incubator containing 5% CO<sub>2</sub> at 37 °C. The experiment was performed in triplicates.

After 3 days, the samples and cover slips were transferred to the wells of a new plate, washed of the residues of the nutrient medium in fresh PBS, and fixed in a 4% paraformaldehyde (PFA) solution for 10 min.

After that, samples and cover slips were washed with fresh PBS and stained with rhodamine-labeled phalloidin (Thermo Fisher Scientific, Waltham, MA, USA) in accordance with the previously developed protocol [21]. Briefly, the samples and cover slips with cells were treated with 0.05% Triton X-100 solution (Amresco, Solon, Cleveland, OH, USA) for 3 min, then washed in PBS thrice. Next, the rhodamine-labeled phalloidin solution in a 1% solution of fetal bovine serum (HyClone Laboratories, Inc., Logan, UT, USA) and PBS (1:500) was added to the wells, incubated for 20 min at room temperature in the dark, and

then washed five times with PBS. Finally, cell nuclei were stained with 4,6-diamidino-2-phenylindole (DAPI, 1:40,000; Sigma-Aldrich, Co., St. Louis, MO, USA) and incubated for 40 s, and then the samples were thoroughly washed with PBS. After painting, the samples were stored in FSB in the dark at +4 °C. Cover glasses with cells from the control wells were mounted on glass slides using a preparation medium (Thermo Fisher Scientific, Waltham, WI, USA) and stored in the dark at room temperature.

Stained MMSCs were studied via fluorescence microscopy with a quantitative and qualitative analysis of adhered cells being performed. The cells were visualized using an Axio Vert inverted fluorescence microscope (Zeiss, Oberkochen, Germany) and a compatible Canon camera (Canon Europa N.V., Amstelveen, The Netherlands). Samples with cells were placed between two glass slides. DAPI fluorescence was recorded using the DAPI filter, and rhodamine-phalloidin fluorescence was recorded using the rhodamine channel. Ten different fields of view of each sample were photographed at  $\times 100$  and  $\times 400$  magnification.

The qualitative analysis consisted of assessing the morphology of MMSCs and their colonies by the stained cytoskeleton. During the quantitative analysis, the size of spheroid colonies on the sample surface was assessed. The counting of cell nuclei on the scaffold surface was not carried out due to the impossibility of accurately determining the number of nuclei in spheroids.

The obtained data were statistically analyzed using the GraphPad Prism software and the nonparametric Mann–Whitney U-test. The results are presented as the mean and the standard deviation (SD).

### 3. Results and Discussion

#### 3.1. FTIR Spectra of the Studied Films

ALG, ALG(CeONP), BC–ALG–CS, and BC–ALG(CeONP)–CS films, as well as citrate-stabilized CeO<sub>2</sub> powder, were studied via FTIR spectroscopy.

In the FTIR spectra of the ALG and ALG(CeONP) films (Figure 1a), one can observe bands in the range of 3400 cm<sup>-1</sup> (OH stretching vibrations), 1595 cm<sup>-1</sup> and 1411 cm<sup>-1</sup> (asymmetric and symmetric stretching vibrations of COO<sup>-</sup> groups), 1090 cm<sup>-1</sup> (glycosidic bond vibrations), and 1026 cm<sup>-1</sup> (C–C stretching vibrations).

When citrate-stabilized CeONPs were introduced into ALG, a shift of the 1090 and 1026 cm<sup>-1</sup> bands by 3–4 cm<sup>-1</sup> was observed (Figure 1b), which may presumably indicate the interaction between ALG and CeONPs.

To obtain more insight into the nature of the interactions in the system under study, a difference spectrum was obtained by subtracting the ALG matrix spectrum from the nanocomposite ALG–CeONP spectrum and comparing the resulting difference spectrum with that of citrate-stabilized CeO<sub>2</sub> (Figure 1c).

In the spectrum of citrate-stabilized CeO<sub>2</sub> in the region of 1800–1200 cm<sup>-1</sup>, there are bands at 1551 cm<sup>-1</sup> and 1390 cm<sup>-1</sup> (asymmetric and symmetric stretching vibrations of the COO<sup>-</sup> group), as well as a shoulder in the region 1700 cm<sup>-1</sup>, which probably refers to the COOH vibrations of citric acid. A pronounced 1730 cm<sup>-1</sup> band and the 1644 and 1440 cm<sup>-1</sup> bands are noticeable in the subtraction spectrum. Such changes in the spectrum of citrate-stabilized CeO<sub>2</sub> may indicate the substitution of citrate by ALG and/or the formation of the additional coordination of the COO<sup>-</sup> group of ALG with cerium ions on the surface of CeONPs. The interaction between ALG and CeONPs is attributed to the presence of coordination vacancies on the surface of CeO<sub>2</sub> [48,49] and the replacement of citrate with ALG can be driven by an entropy effect.

The spectra of BC–ALG–CS and BC–ALG(CeONP)–CS (Figure 2) show the following characteristic absorption bands: a wide band at 3500–3100 cm<sup>-1</sup> (primary and secondary OH groups) and at 1600 cm<sup>-1</sup> and 1422 cm<sup>-1</sup> (asymmetric and symmetric vibrations of the COO<sup>-</sup> group), and vibrations in the 1100 cm<sup>-1</sup> region (glycosidic bond vibrations) and at 1029 cm<sup>-1</sup> (COC stretching vibrations). When citrate-stabilized CeO<sub>2</sub> was introduced into the matrix, the 1728 cm<sup>-1</sup> band was also observed in the spectrum, probably due to the citric acid released. In addition, there were noticeable changes in the shape of the bands



in the  $1100\text{--}1000\text{ cm}^{-1}$  region, in the same region where band shifts were observed when comparing the spectra of ALG and ALG(CeONP) (Figure 2). It can be assumed that this fact also indicates specific interactions of CeONPs with the polysaccharide matrix.

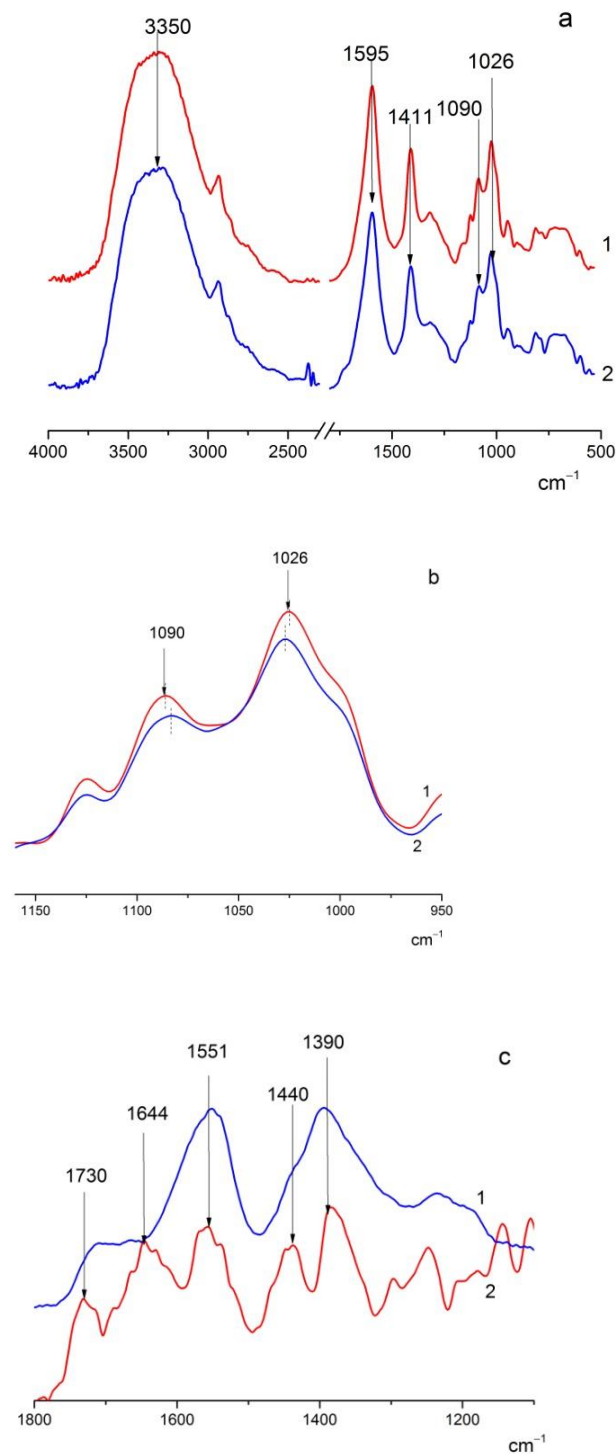


**Figure 1.** FTIR spectra of the studied films. (a): (1) sodium alginate (ALG) and (2) ALG-ceria nanoparticles (CeONPs); (b): fragment of spectra 1a on enlarged scale, ALG (1) and ALG(CeONP) (2); (c): citrate-stabilized  $\text{CeO}_2$  (1) and difference spectrum obtained by subtracting the spectrum of ALG from that of the ALG(CeONP) composite (2).

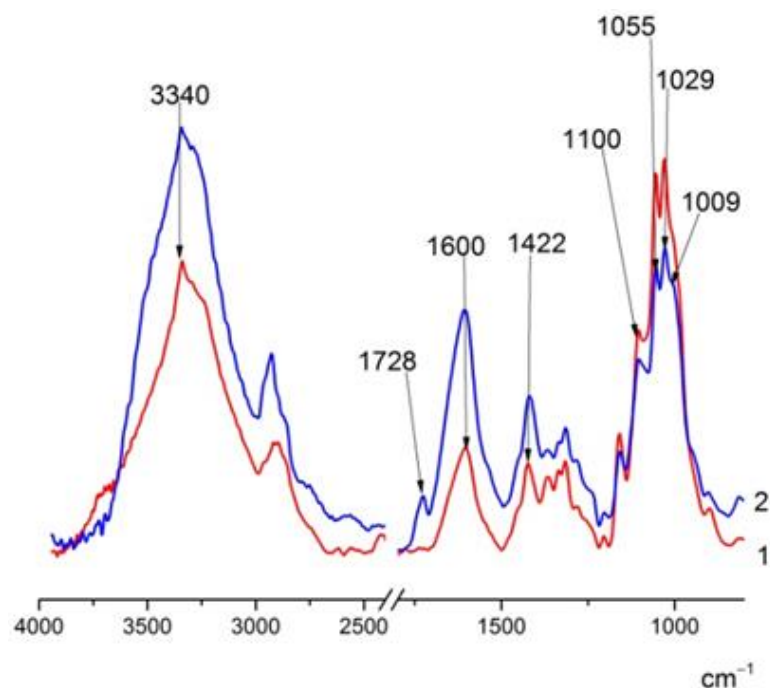


**Figure 2.** FTIR spectra: (1) BC-ALG-chitosan (CS\_), (2) BC-ALG(CeONP)-CS.

### 3.2. Morphology of the Composite Films

Structural features of BC and both types of the BC-based composite films were studied via SEM. The BC-ALG-CS and BC-ALG(CeONP)-CS films were, additionally, tested via energy-dispersive X-ray spectroscopy (EDX). Figure 3 presents SEM images of the investigated films obtained on the films' cryo-cleavages (Figure 3a,c,e) and on the surfaces of the same films (Figure 3b,d,f). The results of the SEM examination of BC and BC-ALG-CS are in agreement with the effects evidenced in our previous work [21]. While analyzing the SEM images of the samples' cross-section, it is evidently seen that the films have a layered structure. In BC (Figure 3a), these layers are divided by the empty galleries of the thickness up to several microns. In both BC-ALG-CS and BC-ALG(CeONP)-CS, this interlayer space is supposed to be filled with the ALG/CS mixture (Figure 3c,e). The inner structure of the composite film filled with CeONPs (Figure 3e) seems to be denser comparing to the unfilled one, without any porosity that can be seen at the cross-section of the BC-ALG-CS film (Figure 3c).

On the surface of the initial BC film (Figure 3b), BC fibrils with diameters up to 100 nm are clearly observed. These fibrils can also be seen on the surface of the BC-ALG(CeONP)-CS film (Figure 3f), but they are partially covered by the surface layer of other polysaccharides, as the surface of the BC-ALG-CS film (Figure 3d) is fully covered by ALG/CS mixture.

The incorporation of CeONPs into the BC-ALG(CeONP)-CS film was confirmed by EDX spectra (Figure 4b).

### 3.3. X-ray Diffraction (XRD) of the Composite Films

Figure 5 shows the XRD patterns of the BC-ALG-CS control film and the corresponding composite film with CeONPs. Both of the patterns reveal two pronounced reflections characteristic of the ordered structure of BC, with intensity maxima in the  $2\theta$  regions of 14 and  $22\text{--}23^\circ$  [50].

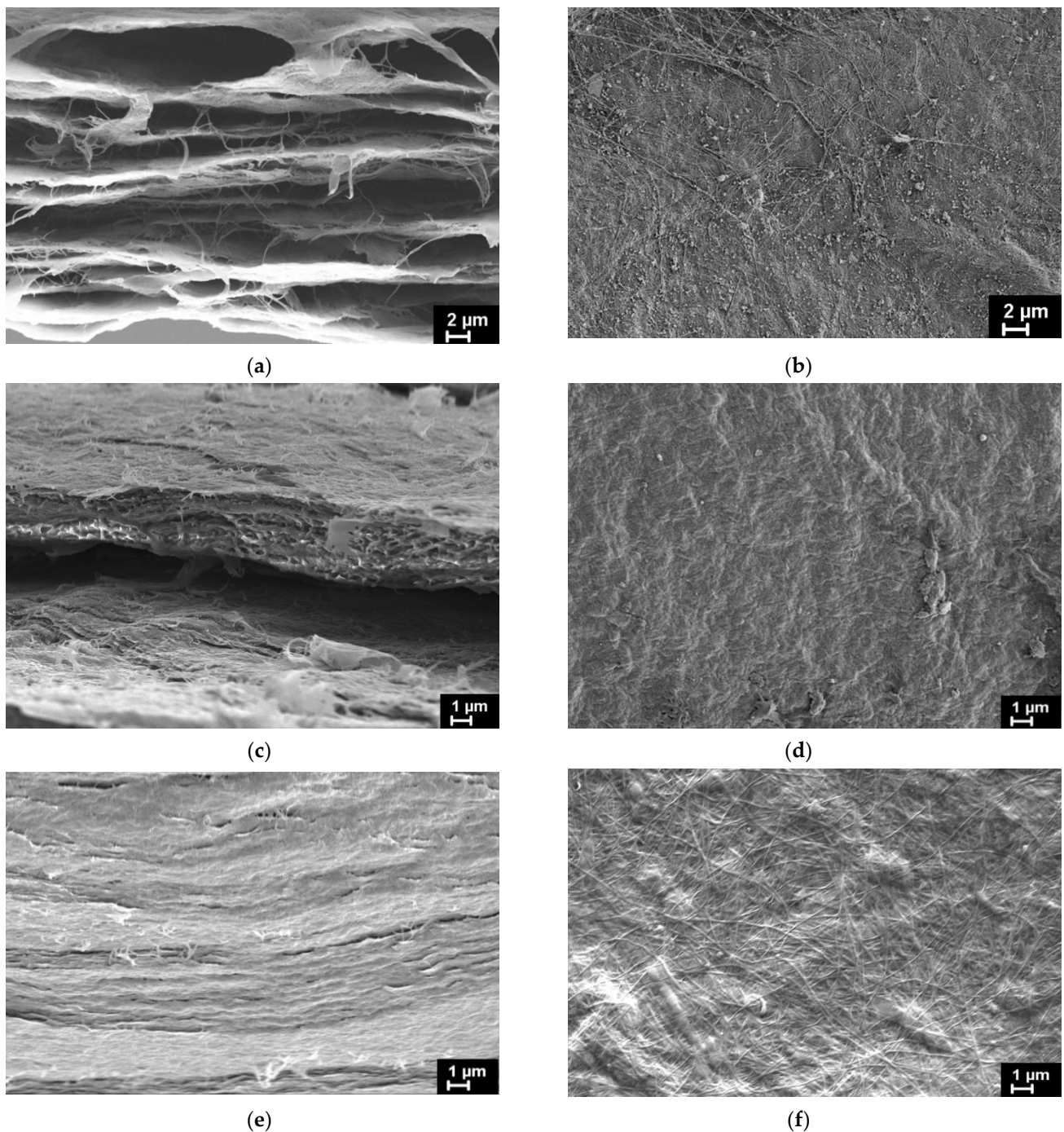


**Figure 3.** SEM images of BC film (a,b), BC-ALG-CS film (c,d), and BC-ALG(CeONP)-CS film (e,f): (a,c,e)—cryo-cleaved surfaces; (b,d,f)—film surfaces.

When comparing the XRD patterns of the BC-ALG-CS control and BC-ALG(CeONP)-CS, one can observe a redistribution of the intensities of these two reflections. For the BC-ALG-CS sample,  $I_{14}/I_{23} = 2.24$ , whereas for the BC-ALG(CeONP)-CS composite,  $I_{14}/I_{22} = 1.36$ . This effect is attributed to a change in the degree of planar orientation of BC macrochains in the sample: in BC-ALG(CeONP)-CS, the planar orientation factor is lower than that in the control BC-ALG-CS film.



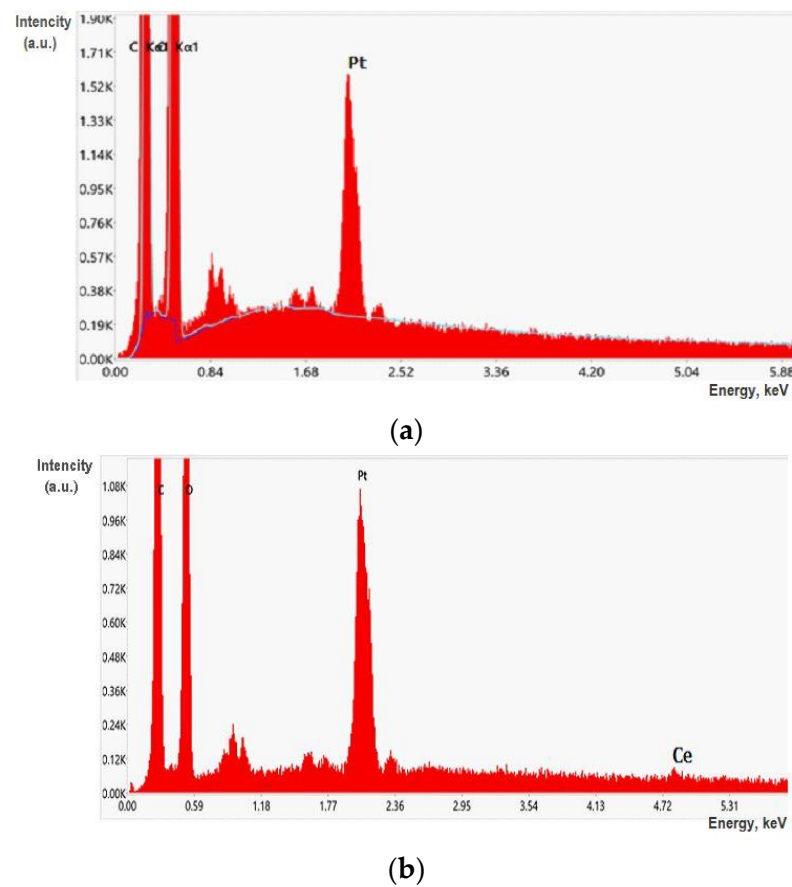


**Figure 4.** EDX spectra registered on the BC-ALG-CS film (a) and the BC-ALG(CeONP)-CS film (b).

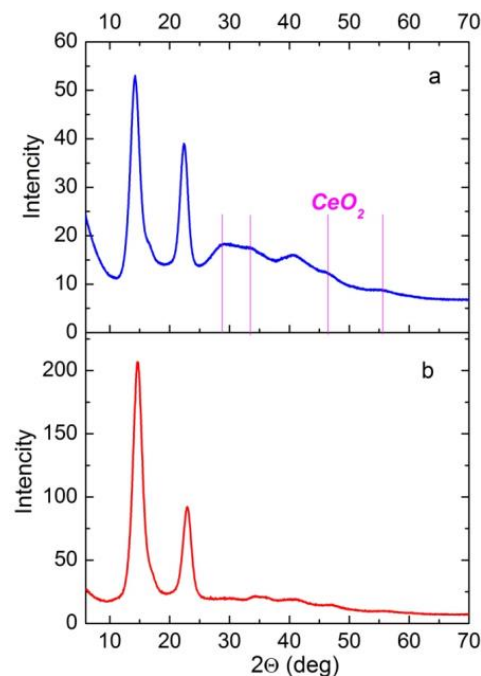


**Figure 5.** XRD patterns of BC-ALG(CeONP)-CS (a) and BC-ALG-CS (b).

In addition to the BC reflections, the XRD pattern of BC-ALG(CeONP)-CS exhibits weak reflections in the regions of  $2\theta = 28.7^\circ, 33^\circ, 47.5^\circ,$  and  $56.3^\circ$ , which correspond to reflections from the  $\text{CeO}_2$  crystal lattice planes (111), (200), (220), and (311), respectively (the cubic fluorite crystal structure: ICDD PDF card #34-394, data from NIST—National Institute

of Standards and Technology, Gaithersburg, MD, USA). When evaluating the intensity of these reflections, one should take into account the fact that for CeONPs in some polymer matrices, the results depend upon the concentration of the filler and the character of the ceria–polymer interaction [43,51–53]. The weak intensity of these reflections in the XRD pattern of the studied nanocomposite may indicate the interaction of ALG with CeONPs.

### 3.4. Swelling of Composite Films in Water

As was demonstrated in [21], the BC–ALG–CS composite, in contrast to the BC sample dried under similar conditions, retained a high degree of swelling in water (Table 1). The introduction of CeONPs into the composition led to an almost two-fold increase in the hydrophilicity of the material. This is most likely to occur as a result of a change in the structure of the ALG layer, due to the interaction between ALG and citrate-stabilized CeONPs.

**Table 1.** Equilibrium swelling of bacterial cellulose (BC), BC–ALG–CS, and BC–ALG(CeONP)–CS films.

Sample	Swelling in Water (g/g)
Bacterial cellulose (BC)	1.9
BC–sodium alginate (ALG)–chitosan (CS)	24.0
BC–ALG–cerium oxide nanoparticles (CeONP)–CS	42.0

### 3.5. Mechanical Properties of the Composite Films

Data on the mechanical properties of the film composite materials are given in Table 2, with the stress–strain curves being presented in Figure 6.

**Table 2.** Mechanical properties of BC, BC–ALG–CS, and BC–ALG(CeONP)–CS films.

Sample	E	$\sigma_b$ (MPa)	$\epsilon_b$ (%)
BC dry	$6.07 \pm 0.18$ GPa	$236 \pm 11$	$4.7 \pm 0.6$
BC–ALG–CS dry	$7.13 \pm 0.08$ GPa	$172 \pm 9$	$4.9 \pm 0.2$
BC–ALG(CeONP)–CS dry	$8.21 \pm 0.53$ GPa	$176 \pm 7$	$3.6 \pm 0.4$
BC–ALG(CeONP)–CS swollen in water	$39 \pm 2$ MPa	$1.9 \pm 0.2$	$4.1 \pm 0.3$

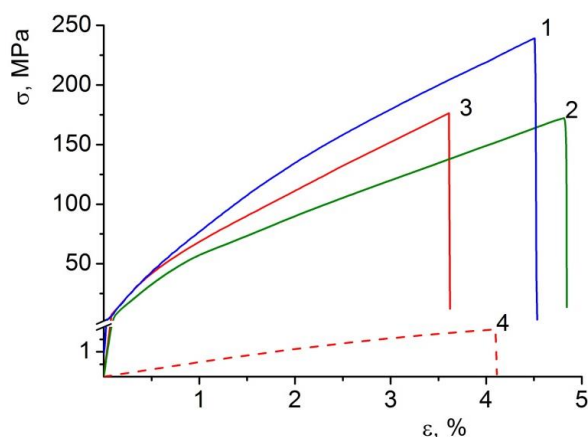


**Figure 6.** Stress–strain curves of (1) BC, (2) BC–ALG–CS, and (3) BC–ALG(CeONP)–CS dry films, and (4) BC–ALG(CeONP)–CS film swollen in water.

Like many polysaccharide films, the examined materials in the dry state are characterized by a high stiffness (elastic modulus 6–8 GPa) combined with a low ultimate deformation (3.6–4.9%). However, such a deformation extent is sufficient for the successful use of the studied films in a number of biomedical applications. Moreover, all the materials possess high-strength characteristics, which are associated precisely with their high stiffness (high elastic modulus, E).

The stiffness of the BC–ALG(CeONP)–CS film exceeds that of the control materials with no CeONPs (the elastic modulus of the composite film is 1.15 times higher than that of the BC–ALG–CS sample). Such an increase in the elastic modulus caused by the introduction of cerium oxide into the polysaccharide matrix clearly indicates the formation of a system of additional intermolecular interactions in BC–ALG(CeONP)–CS (through the surface of the nanoparticles) in addition to those existing in the control polysaccharide material.

Since the films under study were supposed to be used as scaffolds in tissue engineering in a swollen (in aqueous solutions) state, an additional experiment was carried out to determine the mechanical characteristics of the BC–ALG(CeONP)–CS film in an equilibrium swollen state after being stored in water. The storing was performed in the same conditions as those in which moisture absorption was determined (Table 2, Figure 6). It was shown that, even in this case, the BC–ALG(CeONP)–CS composite kept its strength and ultimate deformation at the level of ~2 MPa and 4%, respectively, which is enough for its practical use.

### 3.6. Thermal Analysis of the Composite Films

To ascertain the concentration of cerium oxide in BC–ALG(CeONP)–CS and evaluate its effect on the thermal behavior of the material, a simultaneous thermal analysis of the films (TGA + DTA) was performed.

#### 3.6.1. TGA of the Composite Films

According to TGA data, the thermo-oxidative destruction of all studied films begins in the temperature range of 200–300 °C and ends at 500 °C (Figure 7). When the latter is reached, polysaccharide samples (BC and BC–ALG–CS) are completely degraded, and the degradation products convert to the gas phase (the mass of the sample drops down to ~0). It is worth mentioning that the mass of the BC–ALG(CeONP)–CS sample decreases to 3.6% of the initial value and remains constant upon further heating. After the subtraction of the loss attributed to the evaporation of volatile impurities (5.4%, Table 3) from the total mass loss, we obtain the mass fraction of CeO<sub>2</sub> in the “dry” material that equals to 3.8%.

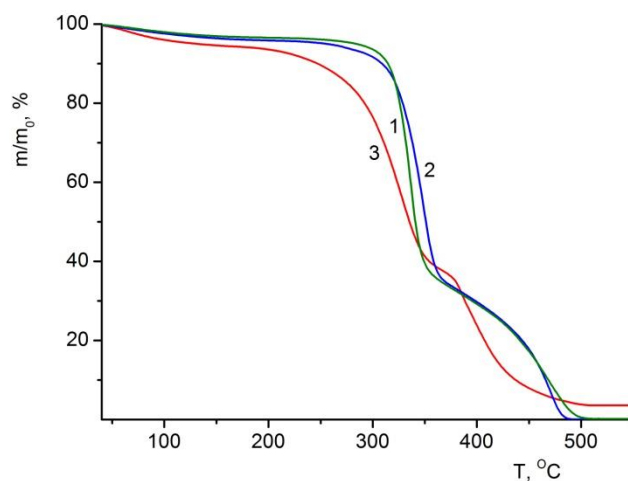


**Figure 7.** TGA curves of (1) BC, (2) BC–ALG–CS, and (3) BC–ALG(CeONP)–CS films.

**Table 3.** Thermal stability indices of BC, BC–ALG–CS, and BC–ALG(CeONP)–CS films in air atmosphere.

Sample	Volatile Impurities, %	Thermal Stability Indices (°C)	
		$\tau_5$	$\tau_{10}$
BC	3.5	310	319
BC–ALG–CS	4.1	304	320
BC–ALG(CeONP)–CS	5.4	251	276

When volatile impurities (3.5–5.5%, Table 3) are eliminated from the samples, the thermal destruction of the films proceeds in two stages, which is typical of a number of polysaccharides. The first (low-temperature) stage occurs in the temperature range of 170–360 °C in the BC–ALG(CeONP)–CS film and at 190–380 °C in the control one. The decomposition processes at these temperatures correspond to the initial stage of pyrolysis, including simultaneous dehydration, depolymerization, and decomposition of monomeric units of polysaccharides. Pyrolysis causes random cleavage of glycosidic bonds, followed by further decomposition resulting in C2-, C3-, and C6-fatty acid formation, including acetic acid and butyric acid. The processes of polymer degradation are completed at the second (high-temperature) stage in the region of 490–500 °C. At this stage, the oligomeric and monomeric products formed at the first stage degrade in an oxygen-containing atmosphere, bringing about the formation of gaseous substances [54–57]. A similar pattern of thermo-oxidative degradation of BC was reported in our previous studies [43].

A comparative analysis of the thermal characteristics of BC–ALG(CeONP)–CS and the control films reveals a pronounced shift to the lower values in the temperature of the thermo-oxidative degradation of the material ( $\tau_5$  and  $\tau_{10}$  drop down by 45–50 °C). This is supposed to result from the introduction of CeONPs into the polysaccharide matrix.

It should be noted that the thermal degradation characteristics of the BC–ALG–CS control film are quite similar to those of the single-component BC film.

### 3.6.2. DTG and DTA of the Composite Films

The same temperature shift in the maximum thermal degradation rate at both stages is also observed on the DTG and DTA curves of the BC–ALG(CeONP)–CS sample (Figure 8a,b). This result agrees well with the data on the catalytic effect of cerium oxide on the destruction processes in organic compounds.

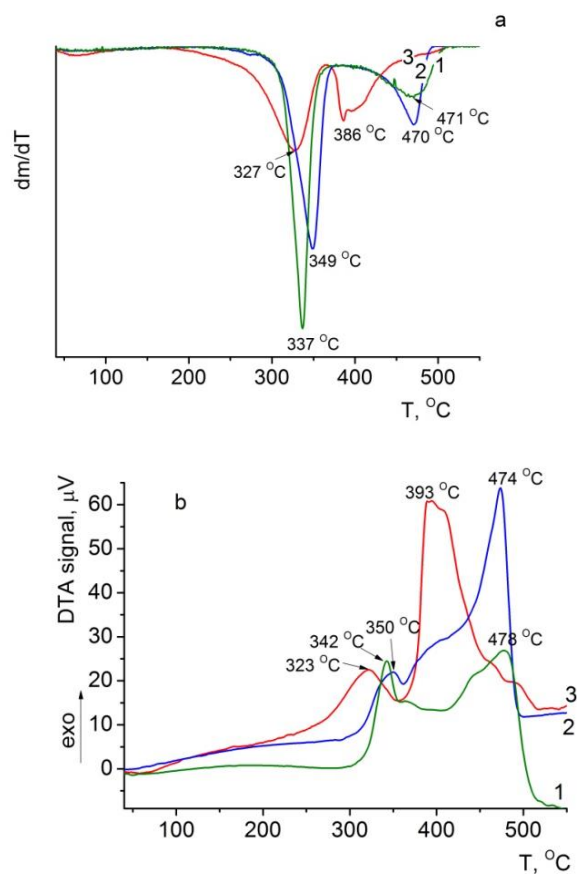


**Figure 8.** DTG (a) and DTA (b) curves of (1) BC, (2) BC–ALG–CS, and (3) BC–ALG(CeONP)–CS films.

### 3.7. Cultivation of Multipotent Mesenchymal Stem Cells (MMSCs)

The cells on the cover glasses were evenly spaced and spread out on the surface of the glass with the formation of a confluent/sub-confluent monolayer, and had a typical elongated shape with multiple outgrowths and clearly detected actin microfilaments. Some of the MMSCs were in the process of division (Figures 9–11). In the case of the BC–ALG–CS, the cells were located evenly on the surface, mainly in the form of a monolayer with a confluence up to 40% with single spheroids. Most of the cells had a typical elongated shape with longitudinal striation and multiple processes, and outgrowths through which they were connected to neighboring cells. A smaller part of the cells on the sample surface had a rounded or close to rounded shape without processes. Spheroids were single with signs of cell migration along the periphery of colonies (Figures 9–11).

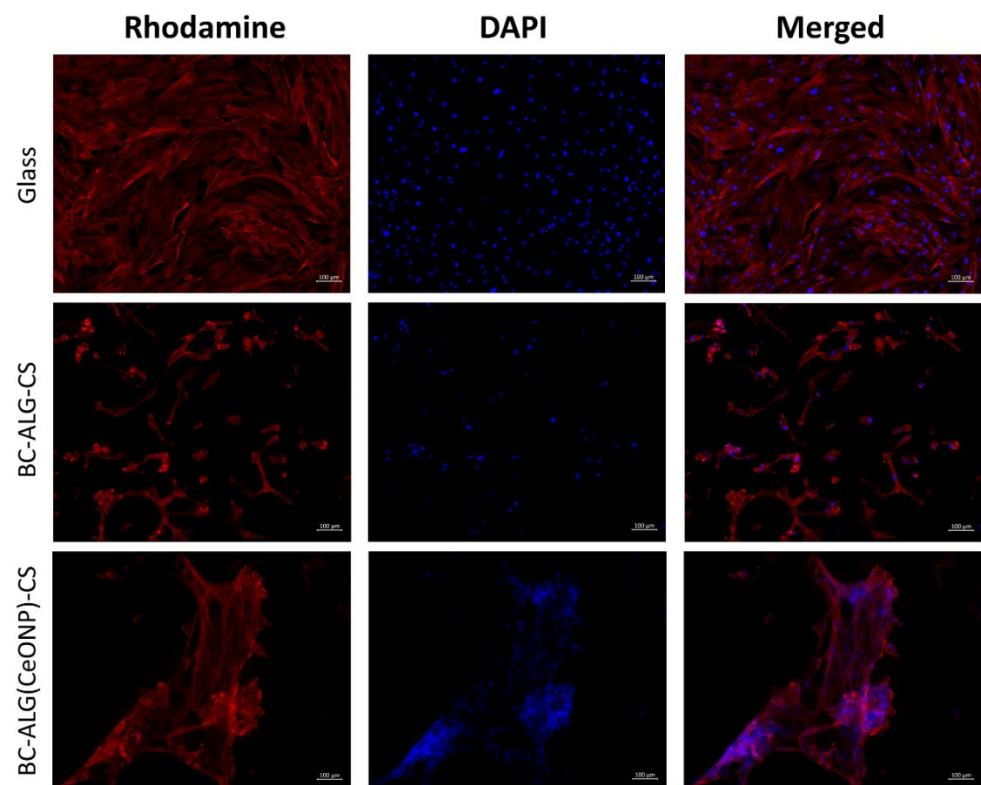


**Figure 9.** Multipotent mesenchymal stem cells adhered to the surfaces of glass and scaffolds. Fibrillar actin of the cytoskeleton was stained with rhodamine fluorochrome; nuclei were stained with DAPI. Combined two-channel image, magnification  $\times 100$ .

In the case of BC–ALG(CeONP)–CS, cells were located superficially and nonuniformly on the scaffold surface in the form of flat colonies, spheroids, and individual cells. In flat colonies, MMSCs had a typical elongated shape with a longitudinal striation more pronounced than in the BC–ALG–CS group and multiple processes. Some cells were in the process of division. The cell density in colonies varied from 30–40 to 80–90% in different areas. Spheroid colonies were detected in small quantities (more than in the BC–ALG–CS group) with signs of active cell migration along the periphery (more pronounced compared to the BC–ALG–CS group). Some of the spheroids were visualized in flat colonies and merged with them due to the pronounced migration of cells from the spheroid colonies. At the same time, there was no statistically significant difference in the maximum longitudinal size of spheroid colonies in both groups of samples ( $p > 0.05$ ) (Table 4). Separately located cells were single, and had a rounded or close to rounded shape without appendages (Figures 9–11).



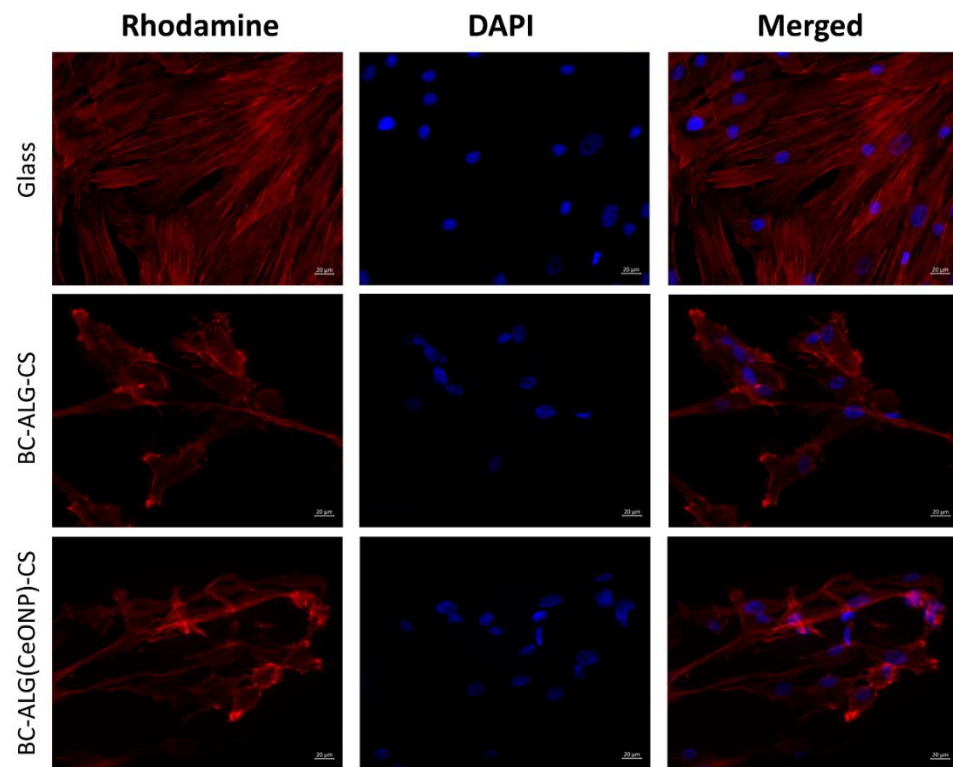


**Figure 10.** Multipotent mesenchymal stem cells adhered to the surfaces of glass and scaffolds. Fibrillar actin of the cytoskeleton was stained with rhodamine fluorochrome; nuclei were stained with DAPI. Combined two-channel image, magnification  $\times 400$ .

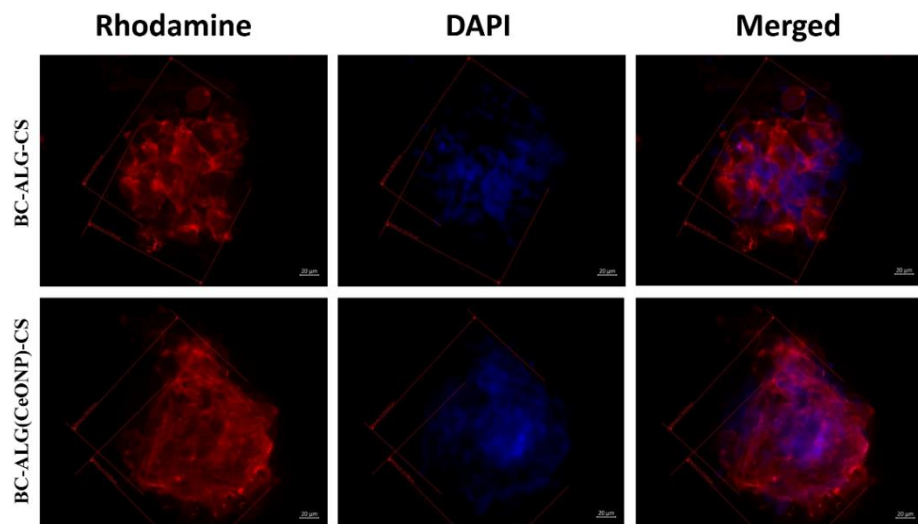


**Figure 11.** Multipotent mesenchymal stem cell spheroids formed on different scaffolds on the third day after seeding. Fibrillar actin of the cytoskeleton was stained with rhodamine fluorochrome; nuclei were stained with DAPI. Combined two-channel image, magnification  $\times 400$ .

The BC-ALG(CeONP)-CS composite film was shown to have better biocompatibility as compared to BC-ALG-CS. This effect can be caused by the complex action of different factors for different reasons. In analyzing these reasons, one should take into account not only the biological activity of the CeONPs, but also the possible action of the nanosized filler upon the physical properties of the matrix material. It is well known that the adhesion of cells to the scaffold surface is strongly affected by the micro-relief and texture of the latter [58]. The introduction of CeONPs into the polysaccharide matrix is supposed to create a surface structure that is most suitable for the formation of contacts of the cell with

the scaffold (see Figure 3f). A certain electric charge on the scaffold surface also ensures optimal conditions for proliferation [3]. In the case of the nanocomposite material formed in our work, this additional electric charge might be provided by the nanoparticles [59].

**Table 4.** Characteristics of multipotent mesenchymal stem cells and cell colonies formed on the surface of the scaffolds on the third day after seeding.

Sample	Nonadhered Cells	Type of Colonies	Maximal Longitudinal Site of Spheroids ( $\mu\text{m}$ )	Cell Migration from Spheroid
Glass	–	monolayer		
BC–ALG–CS	multiple	monolayer+ single spheroids	$154 \pm 2$	+
BC–ALG(CeONP)–CS	single	monolayer+ spheroids	$163 \pm 5$	++

+ and ++ denote the degree of cell migration from spheroid.

A number of studies [34] have found that spheroidal MMSC colonies are formed on the surface of BC matrices. This organization of cell colonies (as compared to the two-dimensional monolayer culture) has a number of features concerning both the process of the formation of aggregates of multicellular spheroids and the properties of the cells composing these spheroids. MMSC spheroids have a better survival compared to single-cell suspensions *in vivo*, but they have a smaller survival advantage than MMSCs when grown under normal conditions of a 2D culture *in vitro* [60]. In living tissue, cells exist in a 3D microenvironment with complex interactions between cells and matrix and with complex dynamics of nutrient and cellular transport [61,62]. The developed BC-based material containing CeONPs showed some advantages over the control when culturing MMSCs *in vitro*, which makes this material promising for *in vivo* applications.

#### 4. Conclusions

A new biocompatible polymeric nanocomposite material for cell engineering and other biomedical applications has been developed and studied. The material, based on bacterial cellulose in combination with sodium alginate and chitosan, contains cerium oxide nanoparticles. For the preparation of the films of the said composition, a step-by-step protocol was optimized, including successive impregnations of pre-pressed bacterial cellulose with a sodium alginate solution containing ceria nanoparticles and with a chitosan solution.

The interaction of the active filler nanoparticles with the polysaccharide matrix in the resulting composite material was corroborated by spectral studies. The results of a comprehensive study of the characteristics of the obtained composite material confirm the effect of nanosized cerium oxide on the properties of polysaccharide films. It is shown that the introduction of the nanoparticles into the polymer composite changes the structure of the material. For instance, the redistribution of the intensities of the two main BC reflections on the diffraction pattern of the nanocomposite reveals a change in the degree of planar orientation of cellulose macrochains.

A change in the network architecture of the polysaccharide composition caused by the introduction of a nanofiller affects the morphology of the composite: according to SEM, the BC-ALG(CeONP)-CS cryo-cleavage is characterized by a denser layered structure compared to the control BC-ALG-CS sample.

Nanocomposite films possess increased hydrophilicity and are characterized by a high elasticity modulus while retaining significant strength, both in dry and swollen states.

The BC-ALG(CeONP)-CS nanocomposite used as a substrate for cell engineering demonstrates an increased intensity in the cultivation process of multipotent mesenchymal stem cells in *in vitro* tests compared to the control BC-ALG-CS sample.

The studies performed have shown that the design of the nanocomposite, based on the intermolecular interactions of polysaccharides and the nanofiller, ensures the biocompatibility of the material and a close similarity to the natural extracellular matrix. The prospects

of using the developed nanocomposite as a material for biomedical purposes are shown. The material can be used for tissue repair and regeneration provided further investigations in this direction are carried out.

**Author Contributions:** Conceptualization, V.A.P., I.V.G. and Y.A.S.; methodology, V.A.P., I.V.G. and A.S.G.; formal analysis, I.V.G. and A.E.B.; investigation, V.A.P., I.V.G., A.S.G., A.I.M., N.V.D., A.K.K., E.M.I., E.N.V. and A.L.N.; resources, A.V.Y., A.L.N. and A.E.B.; writing—original draft preparation, V.A.P., I.V.G. and A.S.G.; writing—review and editing, V.A.P., I.V.G. and Y.A.S.; supervision, A.V.Y. and V.K.I.; project administration, V.A.P. and I.V.G.; funding acquisition, A.V.Y. All authors have read and agreed to the published version of the manuscript.

**Funding:** This work was financially supported by the Russian Science Foundation (project 22-13-00068).

**Institutional Review Board Statement:** The study was conducted according to the guidelines of the Declaration of Helsinki, and approved by the Local Ethics Committee of the Almazov National Medical Research Centre (N<sup>o</sup> 12.26/2014; 1 December 2014). Written informed consent was obtained from all subjects prior to fat tissue biopsy.

**Data Availability Statement:** Data available upon request.

**Acknowledgments:** The authors thank the research associates from the Department of Microbiology, St. Petersburg State University for providing us with bacterial cellulose.

**Conflicts of Interest:** The authors declare no conflict of interest.

## References

1. Madni, A.; Kousar, R.; Naem, N.; Wahid, F. Recent advancements in applications of chitosan-based biomaterials for skin tissue engineering. *J. Bioresour. Bioprod.* **2021**, *6*, 11–25. [[CrossRef](#)]
2. Arkaban, H.; Barani, M.; Akbarizadeh, M.R.; Pal Singh Chauhan, N.; Jadoun, S.; Dehghani Soltani, M.; Zarrantaj, P. Polyacrylic acid nanoplasts: Antimicrobial, tissue engineering, and cancer theranostic applications. *Polymers* **2022**, *14*, 1259. [[CrossRef](#)] [[PubMed](#)]
3. Kalaycıoğlu, Z.; Kahya, N.; Adımcılar, V.; Kaygusuz, H.; Torlak, E.; Akın-Evingür, G.; Erim, F.B. Antibacterial nano cerium oxide/chitosan/cellulose acetate composite films as potential wound dressing. *Eur. Polym. J.* **2020**, *133*, 109777. [[CrossRef](#)]
4. Iijima, K.; Tsuji, Y.; Kuriki, I.; Kakimoto, A.; Nikaido, Y.; Ninomiya, R.; Iyoda, T.; Fukai, F.; Hashizume, M. Control of cell adhesion and proliferation utilizing polysaccharide composite film scaffolds. *Colloids Surf. B Biointerfaces* **2017**, *160*, 228–237. [[CrossRef](#)] [[PubMed](#)]
5. Diaz-Montes, E. Polysaccharides: Sources, Characteristics, Properties, and Their Application in Biodegradable Films. *Polysaccharides* **2022**, *3*, 480–501. [[CrossRef](#)]
6. Andrabi, S.M.; Majumder, S.; Gupta, K.C.; Kumar, A. Dextran based amphiphilic nano-hybrid hydrogel system incorporated with curcumin and cerium oxide nanoparticles for wound healing. *Colloids Surf. B Biointerfaces* **2020**, *195*, 111263. [[CrossRef](#)]
7. Fan, C.; Liao, L.; Zhang, C.; Liu, L. A tough double network hydrogel for cartilage tissue engineering. *J. Mater. Chem. B* **2013**, *1*, 4251–4258. [[CrossRef](#)] [[PubMed](#)]
8. Kalantari, K.; Mostafavi, E.; Saleh, B.; Soltantabar, P.; Webster, T.J. Chitosan/pva hydrogels incorporated with green synthesized cerium oxide nanoparticles for wound healing applications. *Eur. Polym. J.* **2020**, *134*, 109853. [[CrossRef](#)]
9. Raja, I.S.; Fathima, N.N. Gelatin-cerium oxide nanocomposite for enhanced excisional wound healing. *ACS Appl. Bio Mater.* **2018**, *1*, 487–495. [[CrossRef](#)]
10. Weaver, J.D.; Stabler, C.L. Antioxidant cerium oxide nanoparticle hydrogels for cellular encapsulation. *Acta Biomater.* **2015**, *16*, 136–144. [[CrossRef](#)]
11. Lai, W.F.; Tang, R.; Wong, W.T. Ionically crosslinked complex gels loaded with oleic acid-containing vesicles for transdermal drug delivery. *Pharmaceutics* **2020**, *12*, 725. [[CrossRef](#)] [[PubMed](#)]
12. Bhandari, J.; Mishra, H.; Mishra, P.K.; Wimmer, R.; Ahmad, F.J.; Talegaonkar, S. Cellulose nanofiber aerogel as a promising biomaterial for customized oral drug delivery. *Int. J. Nanomed.* **2017**, *12*, 2021–2031. [[CrossRef](#)] [[PubMed](#)]
13. Bahu, J.O.; de Andrade, L.R.M.; de Melo Barbosa, R.; Crivellin, S.; da Silva, A.P.; Souza, S.D.A.; Cárdenas Concha, V.O.; Severino, P.; Souto, E.B. Plant Polysaccharides in Engineered Pharmaceutical Gels. *Bioengineering* **2022**, *9*, 376. [[CrossRef](#)] [[PubMed](#)]
14. Garcia, C.E.G.; Bossard, F.; Rinaudo, M. Electrospun biomaterials from chitosan blends applied as scaffold for tissue regeneration. *Polymers* **2021**, *13*, 1037. [[CrossRef](#)] [[PubMed](#)]
15. Naseri-Nosar, M.; Farzamfar, S.; Sahrpeyma, H.; Ghorbani, S.; Bastami, F.; Vaez, A.; Salehi, M. Cerium oxide nanoparticle-containing poly ( $\epsilon$ -caprolactone)/gelatin electrospun film as a potential wound dressing material: In vitro and in vivo evaluation. *Mater. Sci. Eng. C* **2017**, *81*, 366–372. [[CrossRef](#)]

16. Petrova, V.A.; Chernyakov, D.D.; Poshina, D.N.; Gofman, I.V.; Romanov, D.P.; Mishanin, A.I.; Golovkin, A.S.; Skorik, Y.A. Electrospun bilayer chitosan/hyaluronan material and its compatibility with mesenchymal stem cells. *Materials* **2019**, *12*, 2016. [[CrossRef](#)]
17. Radwan-Pragłowska, J.; Janus, L.; Piatkowski, M.; Bogdal, D.; Matysek, D. Hybrid bilayer pla/chitosan nanofibrous scaffolds doped with zno, fe3o4, and au nanoparticles with bioactive properties for skin tissue engineering. *Polymers* **2020**, *12*, 159. [[CrossRef](#)]
18. Bhattarai, N.; Li, Z.; Edmondson, D.; Zhang, M. Alginate-based nanofibrous scaffolds: Structural, mechanical, and biological properties. *Adv. Mater.* **2006**, *18*, 1463–1467. [[CrossRef](#)]
19. Agarwal, S.; Wendorff, J.H.; Greiner, A. Progress in the field of electrospinning for tissue engineering applications. *Adv. Mater.* **2009**, *21*, 3343–3351. [[CrossRef](#)]
20. Moniri, M.; Boroumand Moghaddam, A.; Azizi, S.; Abdul Rahim, R.; Bin Ariff, A.; Zuhainis Saad, W.; Navaderi, M.; Mohamad, R. Production and status of bacterial cellulose in biomedical engineering. *Nanomaterials* **2017**, *7*, 257. [[CrossRef](#)]
21. Petrova, V.A.; Khripunov, A.K.; Golovkin, A.S.; Mishanin, A.I.; Gofman, I.V.; Romanov, D.P.; Migunova, A.V.; Arkharova, N.A.; Klechkovskaya, V.V.; Skorik, Y.A. Bacterial cellulose (*Komagataeibacter rhaeticus*) biocomposites and their cytocompatibility. *Materials* **2020**, *13*, 4558. [[CrossRef](#)]
22. Ahmed, J.; Gultekinoglu, M.; Edirisinghe, M. Bacterial cellulose micro-nano fibres for wound healing applications. *Biotechnol. Adv.* **2020**, *41*, 107549. [[CrossRef](#)] [[PubMed](#)]
23. Picheth, G.F.; Pirich, C.L.; Sierakowski, M.R.; Woehl, M.A.; Sakakibara, C.N.; de Souza, C.F.; Martin, A.A.; da Silva, R.; de Freitas, R.A. Bacterial cellulose in biomedical applications: A review. *Int. J. Biol. Macromol.* **2017**, *104*, 97–106. [[CrossRef](#)] [[PubMed](#)]
24. Pang, M.; Huang, Y.; Meng, F.; Zhuang, Y.; Liu, H.; Du, M.; Ma, Q.; Wang, Q.; Chen, Z.; Chen, L.; et al. Application of bacterial cellulose in skin and bone tissue engineering. *Eur. Polym. J.* **2020**, *122*, 109365. [[CrossRef](#)]
25. Ul-Islam, M.; Khan, S.; Ullah, M.W.; Park, J.K. Bacterial cellulose composites: Synthetic strategies and multiple applications in bio-medical and electro-conductive fields. *Biotechnol. J.* **2015**, *10*, 1847–1861. [[CrossRef](#)]
26. Khan, S.; Ul-Islam, M.; Ullah, M.W.; Israr, M.; Jang, J.H.; Park, J.K. Nano-gold assisted highly conducting and biocompatible bacterial cellulose-pedot:Pss films for biology-device interface applications. *Int. J. Biol. Macromol.* **2018**, *107*, 865–873. [[CrossRef](#)]
27. Jasim, A.; Ullah, M.W.; Shi, Z.; Lin, X.; Yang, G. Fabrication of bacterial cellulose/polyaniline/single-walled carbon nanotubes membrane for potential application as biosensor. *Carbohydr. Polym.* **2017**, *163*, 62–69. [[CrossRef](#)]
28. Ciechańska, D. Multifunctional bacterial cellulose/chitosan composite materials for medical applications. *Fibres Text. East. Eur.* **2004**, *12*, 69–72.
29. Kim, J.; Cai, Z.; Lee, H.S.; Choi, G.S.; Lee, D.H.; Jo, C. Preparation and characterization of a bacterial cellulose/chitosan composite for potential biomedical application. *J. Polym. Res.* **2011**, *18*, 739–744. [[CrossRef](#)]
30. Krontiras, P.; Gatenholm, P.; Hagg, D.A. Adipogenic differentiation of stem cells in three-dimensional porous bacterial nanocellulose scaffolds. *J. Biomed. Mater. Res. B Appl. Biomater.* **2015**, *103*, 195–203. [[CrossRef](#)]
31. Nakayama, A.; Kakugo, A.; Gong, J.P.; Osada, Y.; Takai, M.; Erata, T.; Kawano, S. High mechanical strength double-network hydrogel with bacterial cellulose. *Adv. Funct. Mater.* **2004**, *14*, 1124–1128. [[CrossRef](#)]
32. Seifert, M.; Hesse, S.; Kabrelian, V.; Klemm, D. Controlling the water content of never dried and reswollen bacterial cellulose by the addition of water-soluble polymers to the culture medium. *J. Polym. Sci. Part A Polym. Chem.* **2004**, *42*, 463–470. [[CrossRef](#)]
33. Yang, J.; Lv, X.; Chen, S.; Li, Z.; Feng, C.; Wang, H.; Xu, Y. In situ fabrication of a microporous bacterial cellulose/potato starch composite scaffold with enhanced cell compatibility. *Cellulose* **2014**, *21*, 1823–1835. [[CrossRef](#)]
34. Woehl, M.A.; Ono, L.; Riegel Vidotti, I.C.; Wypych, F.; Schreiner, W.H.; Sierakowski, M.R. Bioactive nanocomposites of bacterial cellulose and natural hydrocolloids. *J. Mater. Chem. B* **2014**, *2*, 7034–7044. [[CrossRef](#)] [[PubMed](#)]
35. Hosseini, M.; Mozafari, M. Cerium oxide nanoparticles: Recent advances in tissue engineering. *Materials* **2020**, *13*, 3072. [[CrossRef](#)]
36. Krpetic, Z.; Anguissola, S.; Garry, D.; Kelly, P.M.; Dawson, K.A. Nanomaterials: Impact on cells and cell organelles. *Adv. Exp. Med. Biol.* **2014**, *811*, 135–156.
37. Shcherbakov, A.B.; Zholobak, N.M.; Ivanov, V.K. 8-biological, biomedical and pharmaceutical applications of cerium oxide. In *Cerium Oxide (ce<sub>2</sub>): Synthesis, Properties and Applications*; Scire, S., Palmisano, L., Eds.; Elsevier: Amsterdam, The Netherlands, 2020; pp. 279–358.
38. Bhattacharya, D.; Tiwari, R.; Bhatia, T.; Purohit, M.P.; Pal, A.; Jagdale, P.; Mudiam, M.K.R.; Chaudhari, B.P.; Shukla, Y.; Ansari, K.M.; et al. Accelerated and scarless wound repair by a multicomponent hydrogel through simultaneous activation of multiple pathways. *Drug Deliv. Transl. Res.* **2019**, *9*, 1143–1158. [[CrossRef](#)] [[PubMed](#)]
39. Shcherbakov, A.B.; Reukov, V.V.; Yakimansky, A.V.; Krasnopeeva, E.L.; Ivanova, O.S.; Popov, A.L.; Ivanov, V.K. Ce<sub>2</sub> nanoparticle-containing polymers for biomedical applications: A review. *Polymers* **2021**, *13*, 924. [[CrossRef](#)]
40. Rajeshkumar, S.; Naik, P. Synthesis and biomedical applications of cerium oxide nanoparticles—A review. *Biotechnol. Rep.* **2018**, *17*, 1–5. [[CrossRef](#)]
41. Siposova, K.; Huntosova, V.; Shlapa, Y.; Lenkavska, L.; Macajova, M.; Belous, A.; Musatov, A. Advances in the study of cerium oxide nanoparticles: New insights into antiamyloidogenic activity. *ACS Appl. Bio. Mater.* **2019**, *2*, 1884–1896. [[CrossRef](#)]
42. Rozhin, P.; Melchionna, M.; Fornasiero, P.; Marchesan, S. Nanostructured ceria: Biomolecular templates and (bio)applications. *Nanomaterials* **2021**, *11*, 2259. [[CrossRef](#)] [[PubMed](#)]



43. Gofman, I.V.; Nikolaeva, A.L.; Khripunov, A.K.; Ivankova, E.M.; Shabunin, A.S.; Yakimansky, A.V.; Romanov, D.P.; Popov, A.L.; Ermakov, A.M.; Solomevich, S.O.; et al. Bacterial cellulose-based nanocomposites containing ceria and their use in the process of stem cell proliferation. *Polymers* **2021**, *13*, 1999. [[CrossRef](#)] [[PubMed](#)]
44. Arkharova, N.A.; Severin, A.V.; Khripunov, A.K.; Krashennikov, S.V.; Tkachenko, A.A.; Orekhov, A.S.; Davydova, G.A.; Rakova, E.V.; Klechkovskaya, V.V. Composite films based on bacterial cellulose and nanocrystals of hydroxyapatite: Morphology, structure, and properties. *Polym. Sci.-Ser. A* **2019**, *61*, 650–658. [[CrossRef](#)]
45. Ivanova, O.S.; Shekunova, T.O.; Ivanov, V.K.; Shcherbakov, A.B.; Popov, A.L.; Davydova, G.A.; Selezneva, I.I.; Kopitsa, G.P.; Tret'yakov, Y.D. One-stage synthesis of ceria colloid solutions for biomedical use. *Dokl. Chem.* **2011**, *437*, 103–106. [[CrossRef](#)]
46. Petrova, V.A.; Elokhovskiy, V.Y.; Raik, S.V.; Poshina, D.N.; Romanov, D.P.; Skorik, Y.A. Alginate gel reinforcement with chitin nanowhiskers modulates rheological properties and drug release profile. *Biomolecules* **2019**, *9*, 291. [[CrossRef](#)] [[PubMed](#)]
47. Kononova, S.V.; Kruchinina, E.V.; Petrova, V.A.; Baklagina, Y.G.; Klechkovskaya, V.V.; Orekhov, A.S.; Vlasova, E.N.; Popova, E.N.; Gubanova, G.N.; Skorik, Y.A. Pervaporation membranes of a simplex type with polyelectrolyte layers of chitosan and sodium hyaluronate. *Carbohydr. Polym.* **2019**, *209*, 10–19. [[CrossRef](#)]
48. Barteau, M.A. Organic reactions at well-defined oxide surfaces. *Chem. Rev.* **1996**, *96*, 1413–1430. [[CrossRef](#)]
49. Mullins, D.R. The surface chemistry of cerium oxide. *Surf. Sci. Rep.* **2015**, *70*, 42–85. [[CrossRef](#)]
50. Lee, C.M.; Gu, J.; Kafle, K.; Catchmark, J.; Kim, S.H. Cellulose produced by gluconacetobacter xylinus strains atcc 53524 and atcc 23768: Pellicle formation, post-synthesis aggregation and fiber density. *Carbohydr. Polym.* **2015**, *133*, 270–276. [[CrossRef](#)]
51. Passi, M.; Kumar, V.; Packirisamy, G. Theranostic nanozyme: Silk fibroin based multifunctional nanocomposites to combat oxidative stress. *Mater. Sci. Eng. C Mater. Biol. Appl.* **2020**, *107*, 110255. [[CrossRef](#)]
52. Atisme, T.B.; Yu, C.Y.; Tseng, E.N.; Chen, Y.C.; Hsu, P.K.; Chen, S.Y. Interface interactions in conjugated polymer composite with metal oxide nanoparticles. *Nanomaterials* **2019**, *9*, 1534. [[CrossRef](#)] [[PubMed](#)]
53. Bradbury, A.G.W.; Sakai, Y.; Shafizadeh, F. A kinetic model for pyrolysis of cellulose. *J. Appl. Polym. Sci.* **1979**, *23*, 3271–3280. [[CrossRef](#)]
54. de Britto, D.; Campana-Filho, S.P. Kinetics of the thermal degradation of chitosan. *Thermochim. Acta* **2007**, *465*, 73–82. [[CrossRef](#)]
55. López, F.A.; Mercê, A.L.R.; Alguacil, F.J.; López-Delgado, A. A kinetic study on the thermal behaviour of chitosan. *J. Therm. Anal. Calorim.* **2008**, *91*, 633–639. [[CrossRef](#)]
56. Werner, K.; Pommer, L.; Broström, M. Thermal decomposition of hemicelluloses. *J. Anal. Appl. Pyrolysis* **2014**, *110*, 130–137. [[CrossRef](#)]
57. Gubanova, G.N.; Petrova, V.A.; Kononova, S.V.; Popova, E.N.; Smirnova, V.E.; Bugrov, A.N.; Klechkovskaya, V.V.; Skorik, Y.A. Thermal properties and structural features of multilayer films based on chitosan and anionic polysaccharides. *Biomolecules* **2021**, *11*, 762. [[CrossRef](#)]
58. Vesel, A.; Junkar, I.; Cvelbar, U.; Kovac, J.; Mozetic, M. Surface modification of polyester by oxygen- and nitrogen-plasma treatment. *Surf. Interface Anal.* **2008**, *40*, 1444–1453. [[CrossRef](#)]
59. Asati, A.; Santra, S.; Kaittanis, C.; Perez, J.M. Surface-charge-dependent cell localization and cytotoxicity of cerium oxide nanoparticles. *ACS Nano* **2010**, *4*, 5321–5331. [[CrossRef](#)]
60. Tsai, A.C.; Liu, Y.; Yuan, X.; Ma, T. Compaction, fusion, and functional activation of three-dimensional human mesenchymal stem cell aggregate. *Tissue Eng. Part A* **2015**, *21*, 1705–1719. [[CrossRef](#)]
61. Marx, V. Cell culture: A better brew. *Nature* **2013**, *496*, 253–258. [[CrossRef](#)]
62. Pampaloni, F.; Reynaud, E.G.; Stelzer, E.H. The third dimension bridges the gap between cell culture and live tissue. *Nat. Rev. Mol. Cell Biol.* **2007**, *8*, 839–845. [[CrossRef](#)] [[PubMed](#)]